

1

[ATLAS Semivisible Jets]

2

[Elena Laura Busch]

3

Submitted in partial fulfillment of the  
requirements for the degree of  
Doctor of Philosophy  
under the Executive Committee  
of the Graduate School of Arts and Sciences

4

5

6

7

8

COLUMBIA UNIVERSITY

9

2024

10

© 2024

11

[Elena Laura Busch]

12

All Rights Reserved

13

## **Abstract**

14

[ATLAS Semivisible Jets]

15

[Elena Laura Busch]

16

Abstract of dissertation (place-holder).

## Table of Contents

## **List of Figures**

## List of Tables

20

## Acknowledgements

21        Insert your acknowledgements text here. This page is optional, you may delete it if not  
22    needed.

23

## **Dedication**

24

Dedicated to my friends and family

25

## **Introduction or Preface**

26        Insert your preface text here if applicable. This page is optional, you may delete it if not  
27    needed. If you delete this page make sure to move page counter comment in thesis.tex to correct  
28    location.

29

## **Part I**

30

## **Theory**

31

## 32 Chapter 1: The Standard Model

33 The Standard Model of particle physics is a universally accepted framework which explains  
34 the interactions of fundamental particles. All known fundamental particles, outlined in Figure  
35 1.1, are represented in the Standard Model. The model describes three of the four known forces:  
36 the electromagnetic force, the weak force, and the strong force. Gravity, the fourth fundamental  
37 force, is not addressed by the Standard Model. The Standard Model was primarily developed over  
38 the course of the 1960s and 1970s, by combining the work of many physicists into one coherent  
39 model. The Standard Model has been established as a well-tested theory by decades of experimen-  
40 tal physics research.

41 This chapter will seek to introduce the phenomenology and mathematical foundations of the  
42 Standard Model, and present the supporting experimental evidence. Phenomenon which are unex-  
43 plained by the Standard Model such as gravity will be considered at the end of the chapter, leading  
44 to an exploration of theories beyond the Standard Model in the subsequent chapter.

### 45 1.1 Phenomenology: Particles and Forces

#### 46 1.1.1 Particles

47 A classic representation of the particles comprising the Standard Model is shown in Figure  
48 1.1. The two primary particles classes are bosons (gauge bosons and the scalar Higgs boson) and  
49 fermions (leptons and quarks). The bosons are carriers of fundamental forces, while the fermions  
50 are the building blocks of matter. Fermions are sorted into three *generations*, and each fermion is  
51 identified by a unique *flavor*.

52 Each entry in the table in Figure 1.1 is accompanied by 3 characteristic numbers: mass, charge,  
53 and spin. The mass of each particle is determined to limited precision by experimental observation,

## Standard Model of Elementary Particles

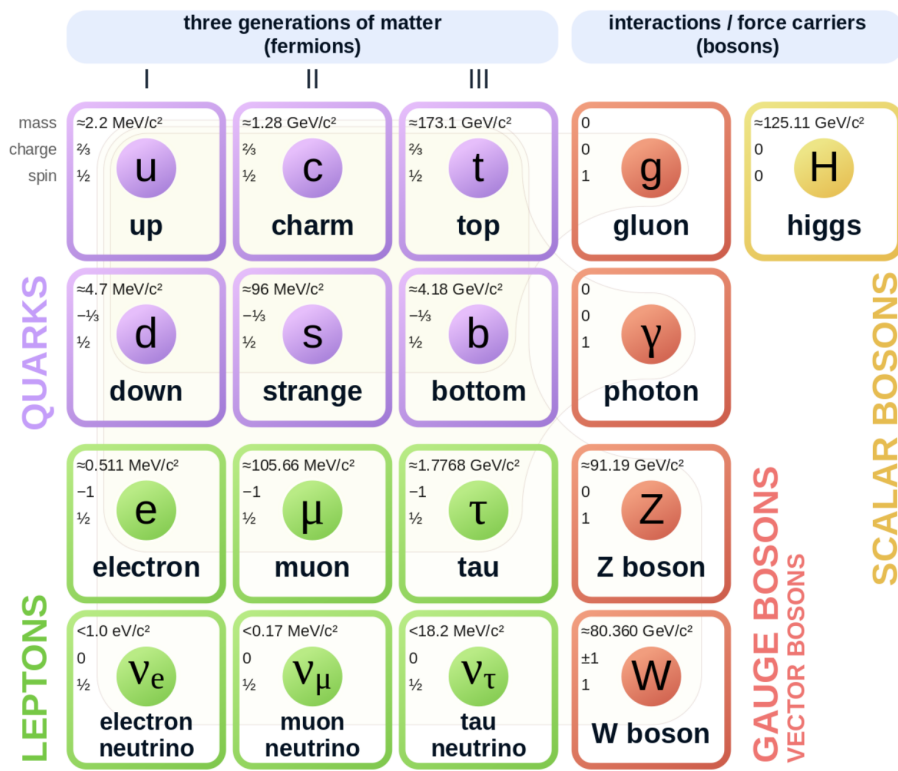


Figure 1.1: Diagram of the 17 particles comprising the Standard Model

54 with the exception of photons and gluons which are known to be massless. Charge refers to the  
55 electromagnetic charge, which is integer for leptons and fractional for quarks. Spin is an intrinsic  
56 form of angular momentum carried by fundamental particles; all fermions have half integer spin,  
57 while bosons have integer spin.

58 Each particle is also known to have an *antiparticle*. Each antiparticle has the same mass but the  
59 opposite charge of their Standard Model counter part; for example, the antiparticle of the electron  
60 is the positron, which has all the same properties but a positive charge. The photon, Z boson,  
61 and Higgs are each their own antiparticle. The nature of antineutrinos is an open question driving  
62 neutrino physics research, as it is not currently known whether neutrinos are their own antiparticle.

63 1.1.2 Forces

64 The three fundamental forces explained by the Standard Model are the electromagnetic force,  
65 the strong force, and the weak force. The photon is the carrier of the electromagnetic force, which  
66 dictates the nature of interactions between electrically charged particles, and is widely covered by  
67 introductory physics courses. The electromagnetic force has an infinite interaction range, a result  
68 of the massless and non-self interaction nature of the photon. The electromagnetic interaction is  
69 described by the theory of quantum electrodynamics (QED).

70 The weak force gives rise to atomic radiation and decay. It allows for the processes of beta  
71 decay, which enables conversion between neutrons and protons within the nucleus of an atom. In  
72 the process of beta decay, a proton decays into a neutron, a positron, and a neutrino; or, a neutron  
73 decays into a proton, an electron and an antineutrino. The weak interaction allows for quark flavor  
74 mixing, the which enables beta decay. The  $W^+$ ,  $W^-$ , and  $Z^0$  are the force carriers of the weak force.  
75 The effective range of the weak force is limited to subatomic distances, as a result of the massive  
76 nature of the mediator bosons. The unified theory of the electroweak interaction posits that at high  
77 enough energies the electromagnetic interaction and the weak force merge into the same force.  
78 This threshold is termed the unification energy and calculated to be about 246 GeV [1].

79 The strong force confines quarks into hadron particles, such as protons and neutrons. The

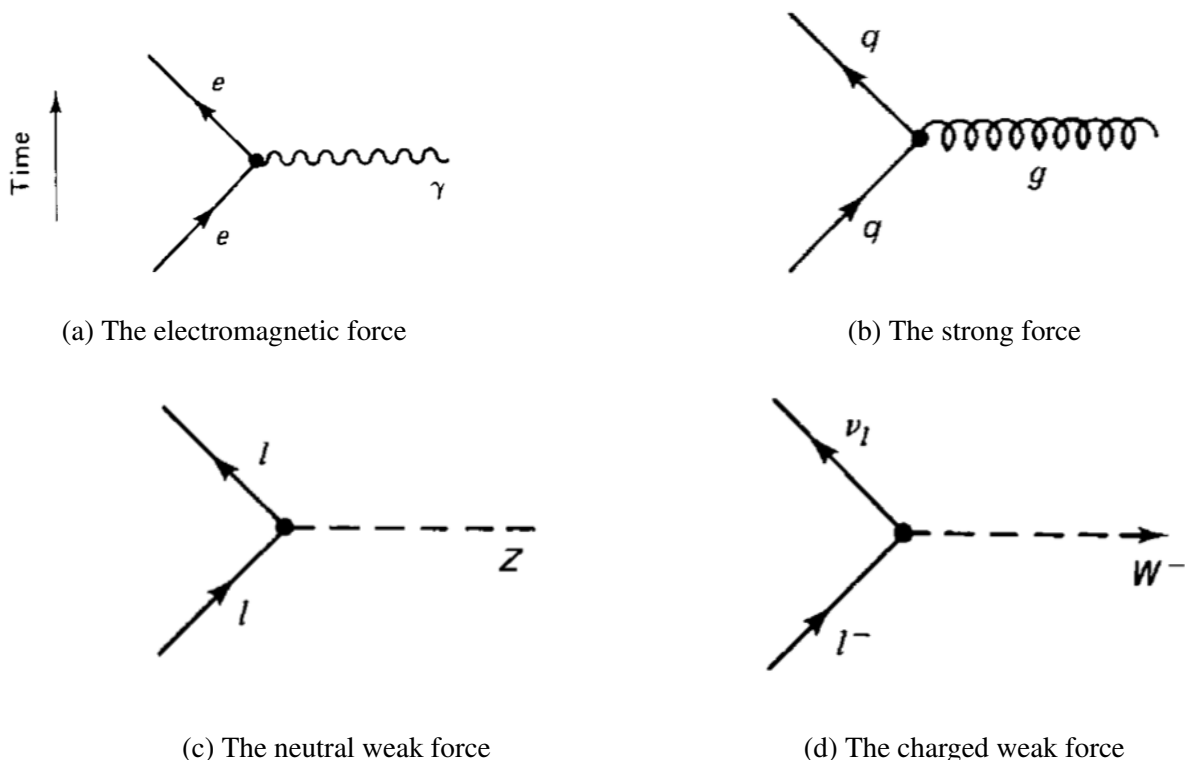


Figure 1.2: Fundamental particle interactions of the three fundamental forces described by the Standard Model [2].

80 strong force also allows for the creation of atomic nuclei by binding protons and neutrons together,  
81 and is generally referred to as the “nuclear force” in this context. The gluon is the mediator of  
82 the strong force, which is a short-range force which acts at subatomic distances on the order of  
83  $10^{-15}$  m. At this range, the strong force is about 100x as strong as the electromagnetic force,  
84 which allows for the creation of positively charged nuclei [2]. The strong force is described by the  
85 theory of quantum chromodynamics (QCD). In the same way that QED dictates the interaction of  
86 electrically charges particles, QCD dictates the interactions of *color-charged* particles. Due to the  
87 particular importance of QCD in this thesis, this topic will be explored in detail in section 1.2.

88 The fundamental Feynmann diagram for each of the three forces discussed here is depicted  
89 in Figure 1.2. The fourth fundamental force, gravity, is not currently explained by any known  
90 mechanism within the Standard Model.

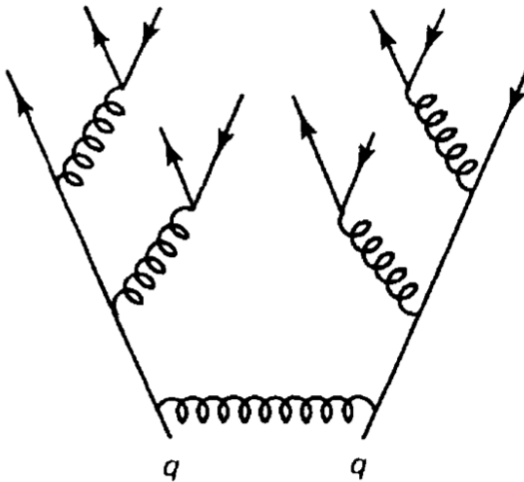


Figure 1.3: An example Feynmann diagram of jet production

## 91 1.2 QCD and Jets

92 While there is only one type of electric charge, there are three types of color charge; red, green,  
 93 and blue. In the process  $q \rightarrow q + g$ , the color of the quark can change. In order to conserve color  
 94 charge, gluons are bicolored, and always carry some positive color charge and some negative color  
 95 charge.

96 Color charged particles can only exist in bound states which result in a neutral total color  
 97 charge, a principle known as confinement. This requires that quarks and gluons exist in group  
 98 states known as hadrons; either mesons in the case of two quarks or baryons in the case of three  
 99 quarks. When a quark is separated from a hadron, confinement dictates that other colored objects  
 100 are produced around the quark to obey confinement. An example of this process is shown in  
 101 Figure 1.3. This ensemble of objects, generally a mixture of quarks and gluons, is termed a *jet*.  
 102 Jets are among the most common phenomenon observed by detectors at hadron colliders, and their  
 103 complex structure makes them a key focus of many physics analyses.

104 **1.3 Symmetries**

105 The Standard Model is a renormalizable quantum field theory that obeys the local symmetry

106  $G_{SM}$ :

$$G_{SM} = SU(3)_C \times SU(2)_L \times U(1)_Y. \quad (1.1)$$

107 The  $SU(3)_C$  symmetry component represents the non-Abelian gauge group of QCD. There  
108 are 8 generators for the  $SU_C(3)$  group which correspond to 8 types of gluon, each representing a  
109 different superposition of color charge [3]. The  $SU(2)_L \times U(1)_Y$  symmetry group represents the  
110 electroweak sector of the Standard Model, which can be spontaneously broken into the electromag-  
111 netic and weak sectors. There are 4 generators for this group, which correspond to four massless  
112 gauge bosons  $W^1$ ,  $W^2$ ,  $W^3$ , and  $B$ . From these massless gauge bosons are formed the massive  
113 mediators of the weak force, the  $W^-$ ,  $W^+$  and  $Z^0$  bosons, and the massless electromagnetic force  
114 carrier, the photon  $\gamma$ . Spontaneous symmetry breaking and the process by which gauge bosons  
115 acquire mass will be addressed in section 1.3.1.

116 Noether's theorem [4] stipulates that any continuous symmetry is associated with a conserved  
117 quantity. In the Standard Model, this means that the  $SU(3)_C$  symmetry gives rise to conservation of  
118 color charge. The  $SU(2)_L \times U(1)_Y$  symmetry gives rise to conservation of electromagnetic charge.  
119 Conservation of spin results from the Poincaré symmetry described by the theory of special rela-  
120 tivity, which combined with Noether's theorem gives us the conservation of energy, momentum,  
121 and angular momentum.

122 The SM Lagrangian is invariant under  $CPT$  symmetry, or charge, parity, and time reversal.  
123 Charge conjugation ( $C$ ) transform a particle into its corresponding antiparticle by reversing the  
124 charge and other quantum numbers. Parity conjugation ( $P$ ) reverses spatial coordinates, which  
125 transforms left-handed particles into right-handed particles and vice-versa. Time reversal ( $T$ ) is  
126 the theoretical process of reversing time. The  $L$  subscript in the  $SU(2)_L$  group indicates that this  
127 symmetry only applies to left-handed fermions. As a result, the  $W^{1,2,3}$  gauge bosons of  $SU(2)_L$

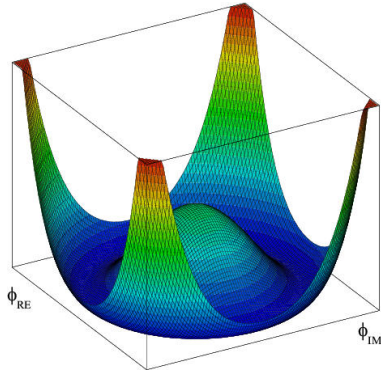


Figure 1.4: An illustration of the “hat shaped” potential of the Higgs field, resulting in a non-zero vacuum expectation value.

only interact with left handed particles, a process which maximally violates P-symmetry in the weak force. A small amount of the CP symmetry violation is also observed in the Standard Model, through the decays of strange flavored mesons [5] and  $b$ -mesons [6]. The CPT theorem posits that the violation of CP symmetry implies that T-symmetry must also be violated, so that CPT is a preserved symmetry.

### 1.3.1 Spontaneous Symmetry Breaking and The Higgs Mechanism

Spontaneous symmetry breaking is the process by which a Lagrangian obeys a symmetry at high energies, but exhibits asymmetric behavior at lower energies. The electroweak symmetry group is spontaneously broken as  $SU(2)_L \times U(1)_Y \rightarrow U(1)_{EM}$ . The quantity conserved by the  $SU(2)_L$  symmetry is weak isospin  $T_{1,2,3}$ , while the quantity conserved by  $U(1)_Y$  symmetry is weak hypercharge  $Y$ . Below very high energies, the presence of the Higgs field causes the electroweak symmetry to break. The Higgs field is a scalar field which forms a complex doublet of the  $SU(2)$  symmetry group, with four degrees of freedom. The shape of the Higgs field potential, shown in Figure 1.4, results in a ground state with a non-zero vacuum expectation value; thus the Higgs field takes a non-zero value throughout all space, which breaks the symmetry of the weak isospin  $SU(2)$  group.

The interaction with the Higgs field mixes the four massless gauge bosons  $W^{1,2,3}$  and  $B$ . Three Higgs field degrees of freedom mix with the massless gauge bosons, resulting in three massive

<sup>146</sup> gauge bosons  $W^-$ ,  $W^+$  and  $Z^0$ . The massless photon  $\gamma$  is created from the components of the  
<sup>147</sup> massless gauge bosons which do not interact with the Higgs field. The scalar Higgs boson arises  
<sup>148</sup> from the one unmixed degree of freedom the Higgs field. Spontaneous symmetry breaking also  
<sup>149</sup> violates the conservation of weak isospin and weak hypercharge, leaving only electromagnetic  
<sup>150</sup> charge ( $Q = T_3 + \frac{1}{2}Y$ ) as a conserved quantity associated with the  $U(1)_{EM}$  symmetry.

## <sup>151</sup> 1.4 Experimental Validation of the Standard Model

<sup>152</sup> The theoretical framework of the Standard Model coalesced into a unified theory in the mid-  
<sup>153</sup> 20th century. A cascade of discoveries providing empirical evidence for the model followed  
<sup>154</sup> closely. In the 1960s, three quarks (up, down and strange) and four leptons (electron, muon,  
<sup>155</sup> and their associated neutrinos) were the known particulate building blocks of matter and the Stan-  
<sup>156</sup> dard Model. The discovery of the charm quark in 1974, through the observation of the  $J/\psi$  meson  
<sup>157</sup> [7][8], confirmed the existence of a fourth quark flavor. The discovery of the  $\tau$  in 1975 [9] provided  
<sup>158</sup> the first evidence of a 3rd generation of matter. This was quickly followed by the observation of  
<sup>159</sup> the  $\Upsilon$  meson in 1977 [10], which provided evidence for the existence of a fifth quark, the  $b$  quark  
<sup>160</sup> (bottom, or beauty). The existence of a 3rd generation of fermion also explained the observation  
<sup>161</sup> of CP violation in the weak force, as it allowed for the addition of a complex phase in the CKM  
<sup>162</sup> matrix (a unitary matrix which describes flavor mixing in the weak interaction). The top quark  
<sup>163</sup> ( $t$ ) and tau neutrino ( $\nu_\tau$ ) were predicted at this point as the final building blocks of three complete  
<sup>164</sup> generations of fermions, and they were discovered by experimental observation around the turn of  
<sup>165</sup> the 21st century [11] [12] [13].

<sup>166</sup> The W and Z bosons were predicted by the Standard Model, but to observe them required the  
<sup>167</sup> construction of a particle accelerator powerful enough to produce them. They were finally observed  
<sup>168</sup> at CERN in 1983 by the UA1 and UA2 experiments [14] [15] at the newly constructed Super Proton  
<sup>169</sup> Synchrotron (SPS). Their masses were observed to be compatible with the masses predicted by the  
<sup>170</sup> Standard Model nearly a decade earlier. The final missing piece then was confirming the existence  
<sup>171</sup> of the Higgs, which again required the construction of a newer and more powerful collider. CERN

172 achieved this with the construction of the Large Hadron Collider (LHC), and in 2012 the ATLAS  
173 and CMS experiments announced the discovery of the Higgs particle [16] [17].

174 **1.5 Limitations of the Standard Model**

175 While the Standard Model has enjoyed decades of experimental results which confirm its pre-  
176 dictions, there are several glaring shortcomings. The observed phenomenon for which the Standard  
177 Model provides no explanation are summarized below.

- 178 • Gravity - the Standard Model does not account for the fourth fundamental force of gravity.
- 179 • Dark Matter - there is no viable candidate to explain the existence of dark matter, a non-  
180 interacting form of matter which must exist to account for gravitational observations which  
181 cannot be explained by general relativity, such as the motion of galaxies, gravitational lens-  
182 ing, and the structure of the universe [18].
- 183 • Matter-Antimatter asymmetry - the level of CP violation in the Standard Model isn't suf-  
184 ficient to explain the large discrepancy between the amount of matter and the amount of  
185 antimatter in the universe today, and the origins of this imbalance are not understood.
- 186 • Neutrino masses - the Standard Model assumes that neutrinos are massless and provides  
187 no mechanism for them to acquire mass. However, observations of neutrino oscillations  
188 indicates they posses some small non-zero mass [19].

189 In addition to these unexplained natural phenomenon, there are several questions about the  
190 *naturalness* of the Standard Model. The principle of naturalness states that dimensionless ratios  
191 between physical constants should be of order 1, and that nature should not be arbitrarily fine-  
192 tuned. While this is largely an aesthetic argument, it points to many aspects of the Standard Model  
193 for which there exists no natural explanation.

- 194 • Strong CP - while CP symmetry is violated in the weak force, observations indicate that it  
195 is preserved by the strong force [20]. The Standard Model predicts that CP violation in the

196 strong force is possible. There is no principle which motivates this incongruity between the  
197 weak force and strong force.

- 198 • Hierarchy Problem - The wide range of masses for elementary particles and the wide range of  
199 scales at which the four fundamental forces operate is not motivated by the SM. Specifically,  
200 it is not understood why the Higgs mass is observed to be well below the Plank scale  $\lambda$ ,  
201 which is the energy level at which the effects of quantum gravity become significant. QFT  
202 indicates that the Higgs mass is determined by contributions from all energy scales including  
203  $\lambda$ , meaning that its observed mass is inexplicably small.

204 The limitations of the Standard Model provide a road map for theoretical and experimental  
205 particle physicists, who seek to develop new theories which account for these observations, and  
206 then to find evidence which might support these *Beyond the Standard Model* (BSM) theories. The  
207 next chapter will introduce the BSM theories which motivate the physics search presented in this  
208 thesis.

## Chapter 2: Physics Beyond the Standard Model

211 In light of the various phenomenon unexplained by the Standard Model, physicists have pro-  
 212 posed various extensions to the Standard Model, collectively termed *Beyond the Standard Model*  
 213 (BSM) theories. A particular focus of the physics programs at the Large Hadron Collider (LHC)  
 214 are BSM models which suggest dark matter candidate particles. If these particles couple to Stan-  
 215 dard Model, they could be produced and observed at the LHC. This chapter will explore Hidden  
 216 Valley models, and in particular the potential for Hidden Valley models to produce *semi-visible*  
 217 *jets*. This will set the theoretical foundations for the experimental search presented in the later  
 218 chapters of this thesis. The mechanisms of dark QCD that arise from these models and allow for  
 219 the production of semi-visible jets will also be discussed.

220 **2.1 Hidden Valley Models**

221 Hidden Valley (HV) models are a category of BSM models that allow for dark matter (DM)  
 222 production at the LHC. They extend the Standard Model with an additional non-Abelian gauge  
 223 group [21]. This introduces the possibility of a complex dark sector, which mirrors the complexities  
 224 of Standard Model QCD, and introduces the possibility of dark quarks and gluons. The term  
 225 “hidden valley” refers to the idea that the DM is hidden from the SM by a high-energy barrier, as  
 226 illustrated in Figure 2.1. The dark sector is assumed to communicate with the Standard Model via  
 227 a “portal”, or “messenger particle”, that can interact with both Standard Model and HV forces. For  
 228 the s-channel scenario, the portal is considered to be a new massive mediator particle  $Z'$ .

229 The portal particle allows for the production of dark sector particles at hadron colliders. If  
 230 dark quarks are produced via the decay  $Z' \rightarrow q_D q_D$  they can hadronize and form dark jets. The  
 231 properties of the dark jets are determined by the dynamics of the dark sector, which are explored in

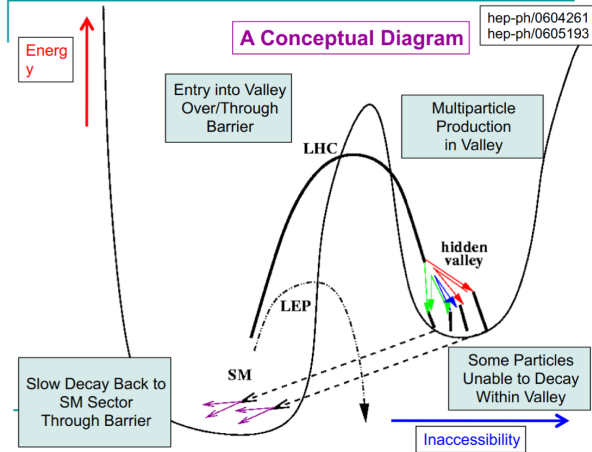


Figure 2.1: Illustration of the hidden valley potential.

232 the subsequent section. Depending on the details of the model, the jets formed by the dark hadrons  
 233 can be categorized as fully dark, semi-visible, leptonic, emerging, or other [21].

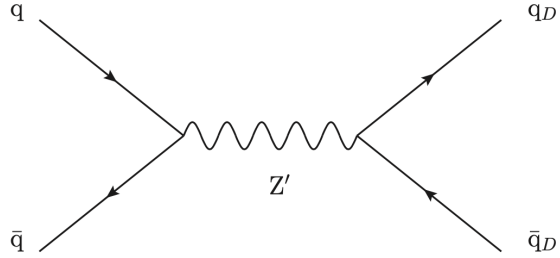


Figure 2.2: The massive mediator particle  $Z'$  of the s-channel realization of a HV model

## 234 2.2 Dark QCD

235 The theoretical underpinning of the semi-visible jet phenomenology is a dark sector with a  
 236 gauge group  $SU(N)_d$  leading to confinement at a scale  $\Lambda_d$ . For illustration, let's consider the  
 237 case of an  $SU(2)_d$  gauge theory, which gives rise to two dark fermionic generations  $\chi_a = \chi_1, \chi_2$ .  
 238 Following the work of Ref [22] we can write the fundamental dark Lagrangian as:

$$\mathcal{L}_{dark} \supset -\frac{1}{2} \text{Tr} G_{\mu\nu}^d G^{d\mu\nu} - \bar{\chi}_a (i\cancel{D} - M_{d,a}) \chi_a \quad (2.1)$$

239        The first term allows for the dark gluons to self-interact, while the second term enables the dark  
240        quarks to hadronize and acquire mass. The dark quarks are assumed to have a common mass  $M_d$ .

241        The coupling strength of the strongly interacting dark quarks is termed  $\alpha_d$ . At the confinement  
242        scale  $\Lambda_d$ , the dark quarks can form bound states. At the scale  $M_d \approx \Lambda_d$  a QCD-like shower occurs.

243        The properties of the hadrons formed by the dark quarks are of particular importance to the  
244        observed dark QCD dynamics. Dark-isospin number  $U(1)_{1-2}$  and dark-baryon number  $U(1)_{1+2}$   
245        are accidental symmetries of the theory which determine the stability of the hadrons. In the case  
246        of two dark flavors, six dark hadrons can be formed: four mesons ( $\chi_1\bar{\chi}_1$ ,  $\chi_2\bar{\chi}_2$ ,  $\chi_1\bar{\chi}_2$ ,  $\bar{\chi}_1\chi_2$ ) and  
247        two baryons ( $\bar{\chi}_1\bar{\chi}_2$ ,  $\bar{\chi}_1\chi_2$ ). The mesons  $\chi_1\bar{\chi}_2$  and  $\bar{\chi}_1\chi_2$  are charged under dark-isospin and will be  
248        stable if this symmetry is unbroken. The baryons would also be stable as they are charged under  
249        the dark-baryon number. These four stable hadrons become dark matter candidates of the theory.

250        The  $\chi_1\bar{\chi}_1$  and  $\chi_2\bar{\chi}_2$  mesons are not charged under either symmetry and are thus expected to decay.  
251        The unstable mesons can decay into stable dark mesons, or into an off-shell  $Z'$ . The off-shell  $Z'$   
252        will then decay into two DM quarks or two SM quarks, and its products will continue to shower  
253        until the final state particles are stable.

254        The number of stable and unstable dark states varies substantially depending on the details  
255        of the model. The model discussed above can be generalized from  $SU(2)_d$  to  $SU(N)_d$ , with any  
256        number of colors  $N_c$  or flavors  $N_f$ . This affects the ratio of possible stable to unstable mesons,  
257        which can directly impact the amount of missing energy. The fraction of missing energy is a  
258        variable in many dark QCD models, and is especially important in the case of semi-visible jets.

### 259        2.3 Semi-visible Jets

260        A “semi-visible jet” occurs when the heavy  $Z'$  messenger particle decays into dark quarks,  
261        which then hadronize in a QCD-like shower. If some of the dark hadrons are stable while others  
262        decay to SM quarks via the off-shell  $Z'$ , a collimated mixture of visible and dark matter is formed  
263        – this is termed a semi-visible jet. If the  $Z'$  messenger particle is produced at rest, the two jets will  
264        be back-to-back in the transverse plane. If there is an imbalance in the amount of invisible particles

265 between the two jets, one of the jets will be observed to be aligned with missing transverse energy.

266 While there are a myriad of HV and dark QCD models, a handful of model parameters are most  
267 important in determining the observable of these showers within a particle detector. The coupling  
268 strength  $\alpha_d$  is one of the most important, as it controls the fraction of dark hadrons emitted in the  
269 shower and their average  $p_T$ . The mass of the dark quarks directly impacts the jet mass. If the  
270 masses of the dark quark flavors are comparable, the ratio of stable to unstable dark hadrons will  
271 be approximately 1:1. However, if there is a mass splitting, stable or unstable dark hadrons may  
272 be favored, which impacts the amount of missing energy observed.

273 The ratio of stable to unstable dark hadrons in the shower is a critical variable for capturing the  
274 behavior of dark showers. This value is termed  $R_{inv}$ :

$$R_{inv} = \frac{\# \text{ of stable hadrons}}{\# \text{ of hadrons}} \quad (2.2)$$

275 Events containing jets aligned with missing transverse momentum are generally considered to  
276 be misreconstructed by other DM searches, and therefore discarded. This class of final states is  
277 therefore largely uncovered by existing DM searches. The nature of the dark hadron shower is  
278 determined by the following parameters: the  $Z'$  mass  $m_{Z'}$ , the  $Z'$  couplings to visible and dark  
279 quarks  $g_q$  and  $g_{q_D}$ , the number of dark colors and flavors, the characteristic scale of the dark sector  
280 confinement  $\Lambda_D$ , the mass scale of the dark hadrons  $m_D$ , and the average fraction of stable hadrons  
281 in the decay  $R_{inv}$ . The coupling to SM quarks determines the  $Z'$  production cross section.

282

## **Part II**

283

## **Experiment**

284

285

## Chapter 3: The Large Hadron Collider

286       The Large Hadron Collider (LHC) is a 26.7 km circular high-energy particle accelerator, span-  
287       ning the Swiss-French border near the city of Geneva, Switzerland [23]. The LHC occupies the  
288       tunnel constructed in 1989 for the Large Electron-Positron (LEP) Collider, and reaches a maxi-  
289       mum depth of 170m below the surface. The LHC is operated by the European Organization for  
290       Nuclear Research (CERN), the largest international scientific collaboration in the world.

291       The LHC accelerates protons and heavy ions, and collides them at four interaction points  
292       around the ring, with a design center-of-mass energy per collision of  $\sqrt{s} = 14$  TeV. Each interaction  
293       point is home to one of four detector experiments, which study the products of the collisions. The  
294       largest of these experiments is the ATLAS detector, a general purpose detector designed to study  
295       the Standard Model and search for new physics that could be produced in LHC collisions [24].  
296       The CMS detector is another general purpose detector, designed and operated independently of the  
297       ATLAS detector, but intended to probe the same range of physics [25]. The ALICE experiment is  
298       a dedicated heavy ion experiment, and the LHC-b experiment is a dedicated *b*-physics experiment  
299       [26] [27].

300       This chapter will cover the multi-component accelerator complex powering the LHC, the state-  
301       of-the-art magnets which steer the particle beams, measurements of the intensity and number of  
302       collisions produced by the LHC, and finally an overview of LHC activities in the past, present, and  
303       future.

304 **3.1 Accelerator Physics**

305 **3.1.1 The Journey of a Proton**

306 From 2010 - 2018, the protons which fed the LHC started as hydrogen gas. The electrons were  
307 removed from the hydrogen atoms through the use of strong electric fields. The linear accelerator  
308 LINAC2 then accelerated the protons to an energy of 50 MeV. Between 2018 and 2020, LINAC2  
309 was replaced with LINAC4, which instead accelerates  $H^-$  ions, hydrogen atoms with two electrons.  
310 LINAC4 is capable of accelerating the  $H^-$  ions to 160 MeV. Before injection to the next part of  
311 the acceleration chain, both electrons are stripped from the  $H^-$  ions, leaving just protons. From  
312 here the protons enter the Proton Synchrotron booster, where they are accelerated up to 1.4 GeV of  
313 energy. Subsequently they are sorted into bunches separated in time by 25 ns, where each bunch  
314 contains approximately  $10^{11}$  protons. Next the bunches pass through the Proton Synchrotron (PS)  
315 and the Super Proton Synchrotron (SPS), where they reach energies of 25 GeV and 450 GeV  
316 respectively. Finally they are injected into the LHC as two beams traveling in opposite direction.  
317 The original design allowed each beam to be accelerated up to 7 TeV of energy. Due to limitations  
318 in the performance of the superconducting LHC magnets, the highest energy actually achieved by  
319 the LHC beams during Run 2 was 6.5 TeV, giving a collision center-of-mass energy of  $\sqrt{s} = 13$   
320 TeV [28]. Figure 3.1 shows the full LHC accelerator complex.

321 Acceleration in the LHC is performed by eight radio frequency (RF) cavities located around the  
322 ring. Each RF cavity produces a 2 MV electric field oscillating at 40 MHz. The 40MHz oscillation  
323 produces a point of stable equilibrium every 2.5 ns. These points of equilibrium are synchronized  
324 with the occurrence of the proton bunches produced in the PS – a proton bunch occupies one out  
325 of every ten points of stable equilibrium, such that the bunches maintain a 25 ns spacing [28].

326

## The CERN accelerator complex Complexe des accélérateurs du CERN

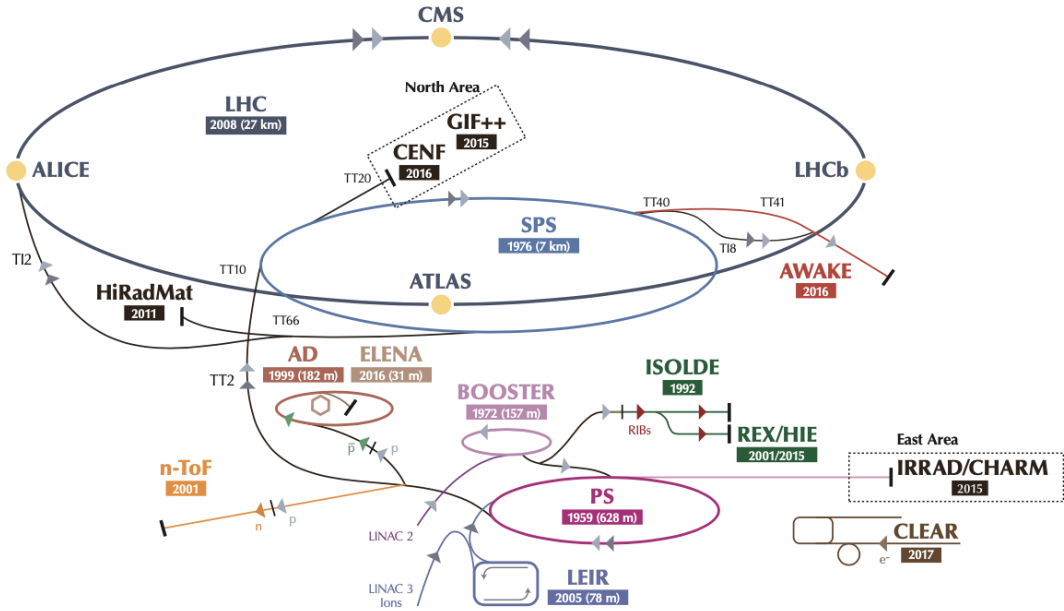


Figure 3.1: The LHC accelerator complex at CERN [29]

### 327 3.1.2 Magnets

328 In addition to the acceleration cavities, the LHC houses 9593 superconducting magnets which  
 329 direct and focus the proton beam on its 27 kilometer journey. The magnets are comprised of super-  
 330 conducting Niobium-Titanium coils cooled to 1.9K by superfluid helium. As the beams approach  
 331 one of the four collision points around the ring, multipole magnets focus and squeeze the beam for  
 332 optimal collisions [28].

333 The LHC is divided into sections, where each section contains an arc and a straight insertion. The arcs are composed of 1232 large dipole magnets which bend the beam  
 334 to follow the roughly circular 27 km path. The main dipoles generate powerful 8.3 tesla magnetic  
 335 fields to achieve this bend. Each dipole magnet is 15 meters long and weighs 35 tonnes. The  
 336 dipoles work in conjunction with quadrupole magnets, which keep the particles in a focused beam,  
 337 and smaller sextupole, octupole and decapole magnets which tune the magnetic field at the ends of  
 338 the dipole magnets [30].

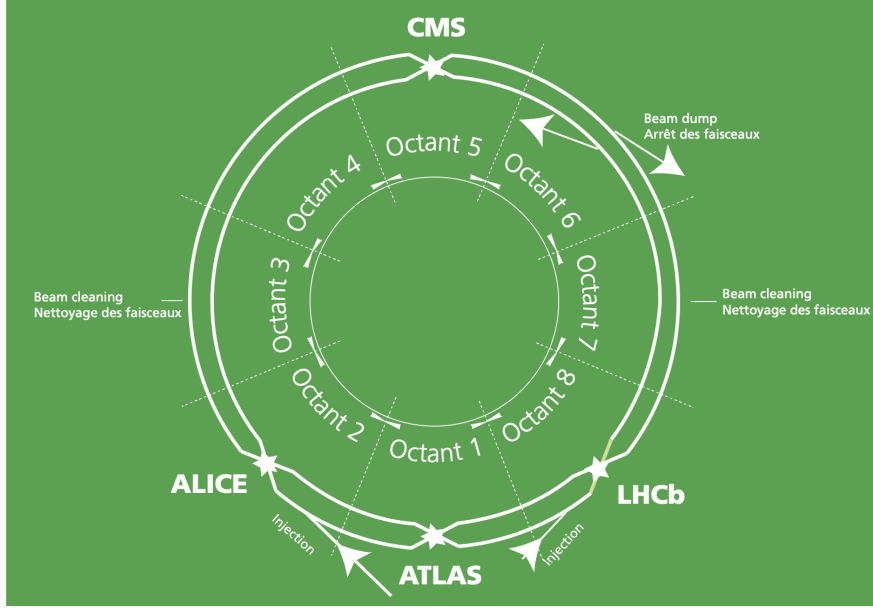


Figure 3.2: The octants of the LHC and location of various beam activities [28]. Stars indicate the locations of beam collisions, and the associated detectors recording the outcome of those collisions.

340        The straight insertion sections have different purposes depending on their location around the  
 341        ring: beam collisions, beam injection, beam dumping, or beam cleaning. At the four collision  
 342        points, insertion magnets squeeze the beam to ensure a highly focused collision. This is accom-  
 343        plished with a triplet of quadrupole magnets, which tighten the beam from 0.2 millimeters to just  
 344        16 micrometers in diameter. Insertion magnets also clean the beam, which prevents stray particles  
 345        from hitting sensitive components throughout the LHC. When the LHC is ready to dispose of a  
 346        beam of particles, beam dump magnets deflect the path of the beam into a straight line towards  
 347        a block of concrete and graphite that stops the beam. A dilution magnet then reduces the beam  
 348        intensity by a factor of 100,000 before the final stop [30]. Figure 3.2 shows the locations various  
 349        beam activities.

350        **3.2 Luminosity**

351        Collisions at the LHC occur when the two beams of proton bunches cross at one of the four  
 352        interaction points. The intensity of collisions is described by the instantaneous luminosity, the

353 formula for which is given in equation 3.1.

$$L = \frac{fN_1N_2}{4\pi\sigma_x\sigma_y} \quad (3.1)$$

354 Here  $f$  is the revolution frequency,  $N_1$  and  $N_2$  are the number of particle per bunch for each  
355 beam, and  $\sigma_x$ ,  $\sigma_y$  are the horizontal and vertical beam widths.

356 The instantaneous luminosity gives the number of the collisions that could be produced at the  
357 interaction point per unit of cross-sectional area per unit of time, generally expressed in  $\text{cm}^{-2}\text{s}^{-1}$ .  
358 The integrated luminosity is obtained by integrating the instantaneous luminosity over a given  
359 block of time, and measures the total number of collisions which have occurred during that op-  
360 eration period. The total integrated luminosity is directly correlated with the size of the datasets  
361 collected by the LHC experiments. Total integrated luminosity for Run 2 is illustrated in Figure  
362 3.3.

363 High levels of instantaneous luminosity result in multiple  $pp$  collisions per bunch crossing,  
364 which leads to an effect known as *pileup*. Pileup poses a challenge for detector physics, as recon-  
365 structing the products of multiple simultaneous events is far more challenging than reconstructing  
366 a single event with no pileup. Pileup conditions vary from year-to-year and run-to-run of LHC op-  
367 eration, and the impact of these conditions are taken into account when analyzing the data, as will  
368 be discussed further in Chapter 5. Measurement of pileup conditions during Run 2 are illustrated  
369 in Figure 3.3.

370 The design peak luminosity of the LHC is  $1.0 \times 10^{34} \text{ cm}^{-2}\text{s}^{-1}$ . During Run 1 of the LHC the  
371 peak instantaneous luminosity was  $0.8 \times 10^{34} \text{ cm}^{-2}\text{s}^{-1}$ . Over the course of Run 1 the LHC collected  
372 a total integrated luminosity of  $5.46 \text{ fb}^{-1}$  at  $\sqrt{s} = 7 \text{ TeV}$ , and  $22.8 \text{ fb}^{-1}$  at  $\sqrt{s} = 8 \text{ TeV}$ . Following the  
373 first long shutdown and upgrade phase of operations, the LHC achieved a center of mass energy  
374  $\sqrt{s} = 13 \text{ TeV}$  at the beginning of Run 2 in 2015. The LHC was also able to deliver  $2.0 \times 10^{34}$   
375  $\text{cm}^{-2}\text{s}^{-1}$  peak instantaneous luminosity, double the design value. During LHC Run 2, from 2015-  
376 2018, the LHC delivered  $156 \text{ fb}^{-1}$  of integrated luminosity for proton-proton collisions. Run 3 of

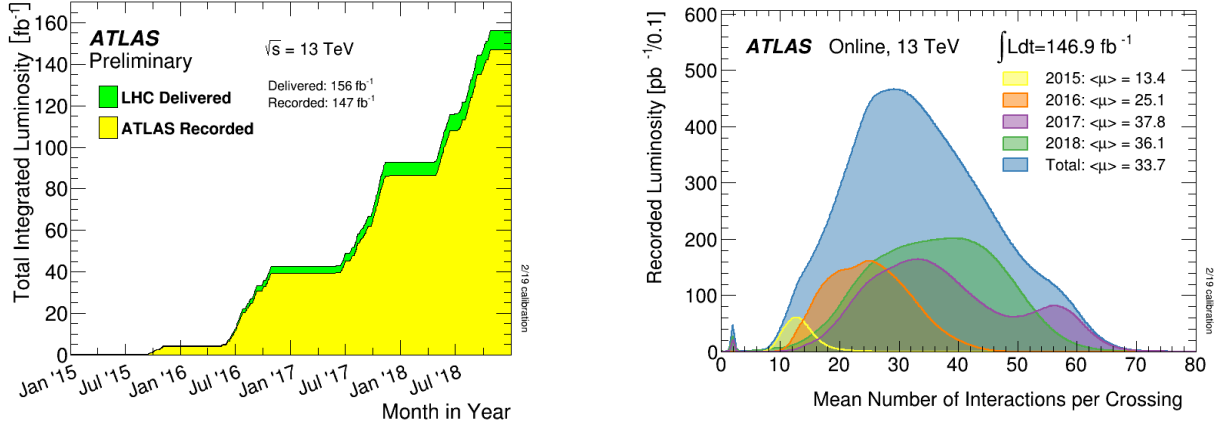


Figure 3.3: (Left) Total integrated luminosity over the course of Run 2. (Right) Average number of  $pp$  interactions per bunch crossing in Run 2. Each curve is weighted by the integrated luminosity for the year.

<sup>377</sup> the LHC began in 2022, and is expected to deliver  $250 \text{ fb}^{-1}$  of integrated luminosity to the ATLAS  
<sup>378</sup> and CMS experiments by 2026 [31].

<sup>379</sup> The goal of LHC physic analyses is to find and study rare events produced by interesting  
<sup>380</sup> physics processes. The cross section  $\sigma$  of a given process indicates the probability of that process  
<sup>381</sup> occurring given the beam conditions of the LHC. Multiplying the cross section by the integrated  
<sup>382</sup> luminosity of a dataset gives the expected number of events for that process within the dataset.

$$N_{\text{events}} = \int \sigma L(t) dt = \mathcal{L} \times \sigma \quad (3.2)$$

<sup>383</sup> The cross section for most processes of interest, especially BSM processes, is several orders of  
<sup>384</sup> magnitude below the total cross section for the LHC. Therefore maximizing the number of events  
<sup>385</sup> produced in collisions is crucial to increase the likelihood of producing events from processes of  
<sup>386</sup> interest. For this reason, maximizing instantaneous luminosity is a key factor in accelerator design  
<sup>387</sup> and operation, while mitigating the resulting pileup effects is a key component in detector design  
<sup>388</sup> and operation.

389    **3.3 LHC Timeline**

390    The first proton-proton collisions at the LHC were achieved in 2010 with a center-of-mass  
391    energy of  $\sqrt{s} = 7$  TeV. Run 1 of the LHC took place between 2010 and early 2013, during which  
392    time the center-of-mass collision energy increased from 7 TeV to 8 TeV. Figure 3.4 shows an  
393    overview of LHC activities beginning in 2011, in the midst of Run 1. The data collected during  
394    Run 1 led to the discovery of the Higgs Boston in 2012 [32].

395    Between 2013 and 2015 the LHC underwent the first Long Shutdown (LS1) during which  
396    time maintenance and renovation was performed on the accelerator chain, including the repair and  
397    consolidation of the high-current splices which connect the super-conducting LHC magnets. Run  
398    2 of the LHC took place from 2015 to 2018 and achieved a center-of-mass energy of  $\sqrt{s} = 13$  TeV.  
399    Analysis of data collected in Run 2 is still on going, and is the subject of study in this thesis.

400    Between 2018 and 2022 the LHC underwent the second Long Shutdown (LS2), allowing for  
401    further detector and accelerator maintenance and upgrades. Key improvements to the LHC in-  
402    cluded the improvement of the insulation for over 1200 diode magnets, and the upgrade from  
403    LINAC2 to LINAC4 mentioned in Section 3.1.1. Run 3 of the LHC began in 2022 and achieved a  
404    center-of-mass energy of  $\sqrt{s} = 13.6$  TeV.

405    Run 3 is scheduled to continue through 2026, at which point the LHC machine and detectors  
406    will undergo upgrades for the *high luminosity* LHC (HL-LHC). The HL-LHC will increase the  
407    instantaneous machine luminosity by a factor of 5 - 7.5 with respect to the nominal LHC design.  
408    The bottom panel of Figure 3.4 shows an overview of the preparation work for the HL-LHC that  
409    has been going on concurrently with Run 1, 2, and 3 of the LHC [33].



Figure 3.4: Timeline of LHC and HL-LHC activities [31]. Integrated luminosity estimates are approximate, and not reflective of the exact amount delivered to each experiment.

410

411

## Chapter 4: The ATLAS Detector

412     The ATLAS detector (**A Toroidal LHC ApparatuS**) is one of two general purpose physics  
413   detectors designed to study the products of proton-proton collisions at the LHC. The detector is  
414   composed of a variety of specialized subsystems, designed to fully capture a wide array of physics  
415   processes. The apparatus is 25m high, 44m in length, and weighs over 7000 tons [34]. The LHC  
416   beam pipes direct proton beams to an interaction point at the center of ATLAS, and the cylindrical  
417   detector design captures a complete 360° view of the *event*, tracking all particles that result from  
418   the collision.

419     The main components of the ATLAS detector are the Inner Detector (ID) which provides high  
420   precision tracking of charged particles leaving the collision vertex, the calorimeter system which  
421   measures the energy of electromagnetic and hadronic objects, and the Muon Spectrometer (MS)  
422   which gives detailed information about muons that reach the outer radii of the detector. Two  
423   magnet systems, a 2 T solenoid magnet surrounding the ID, and a 0.5-1.0 T toroid magnet system  
424   situated throughout the MS, produce magnetic fields which bend the trajectory of charged particles  
425   traversing the detector. In addition to the main detector components, dedicated forward detectors  
426   monitor beam conditions and instantaneous luminosity, and an online trigger system reduces the  
427   data rate to a manageable level for storage. Each of these components will be discussed in further  
428   detail in this chapter.

### 429   **4.1 Coordinate System and Geometry**

430     The ATLAS detector employs a right hand cylindrical coordinate system. The  $z$  axis is aligned  
431   with the beam line, and the x-y plane sits perpendicular to the beam line. The coordinate system  
432   origin is centered on the detector, such that the origin corresponds with the interaction point of the

433 two colliding beams. The detector geometry is usually characterized by polar coordinates, where  
434 the azimuthal angle  $\phi$  spans the x-y plane. The polar angle  $\theta$  represents the angle away from the  
435 beam line, or  $z$  axis.  $\theta = 0$  aligns with the positive  $z$ -axis, and  $\phi = 0$  aligns with the positive x-axis.

436 The polar coordinate  $\theta$  is generally replaced by the Lorentz invariant quantity *rapidity* or  $y$ :

$$y = \frac{1}{2} \ln\left(\frac{E + p_z}{E - p_z}\right). \quad (4.1)$$

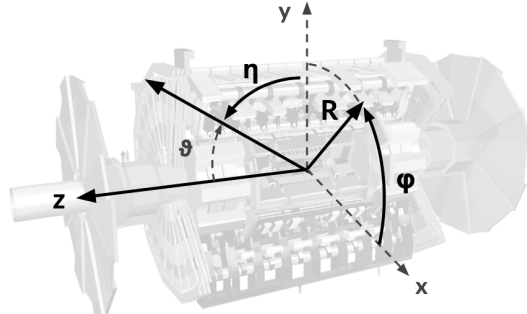
437 This substitution is advantageous because objects in the detector are traveling at highly rela-  
438 tivistic speeds. The relativistic speed also means that the masses of the particles are generally small  
439 compared to their total energy. In the limit of zero mass, the rapidity  $y$  reduces to the pseudorapid-  
440 ity  $\eta$ , which can be calculated directly from the polar angle  $\theta$ :

$$\eta = -\ln\left(\frac{\theta}{2}\right). \quad (4.2)$$

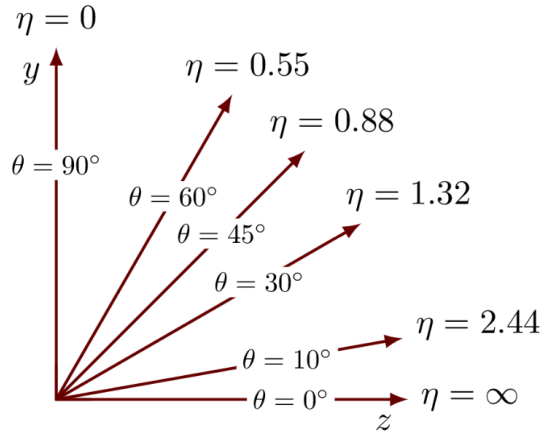
441 The distance between physics objects in the detector is generally expressed in terms of the solid  
442 angle between them  $\Delta R$ :

$$\Delta R = \sqrt{\Delta\phi^2 + \Delta\eta^2} \quad (4.3)$$

443 Figure 4.1a depicts the orientation of the coordinate system with respect to the ATLAS detector,  
444 while Figure 4.1b illustrates the relationship between  $\theta$ ,  $\eta$ , and the beamline axis  $z$ . Direct or “head  
445 on” proton-proton collisions are more likely to result in objects whose momentum is directed  
446 along transverse plane (low  $|\eta|$ ); glancing proton-proton collisions are more likely to result in  
447 objects whose momentum is directed along the  $z$ -axis (high  $|\eta|$ ). Due to the difference in the  
448 nature of these collisions, as well as the cylindrical design of the ATLAS detector, the detector  
449 is divided into regions of low and high  $\eta$ . Each subsystem has a “central” or “barrel” region  
450 covering low  $|\eta|$ , while the “forward” or “end-cap” regions cover the area up to  $|\eta| = 4.9$ . Each of  
451 the three main ATLAS subsystems will be discussed in the following sections.



(a) The ATLAS geometry



(b) Relationship between  $\eta$  and  $\theta$

Figure 4.1: ATLAS coordinate system and geometry

## 452 4.2 Inner Detector

453        The Inner Detector (ID) is the ATLAS subsystem closest to the interaction point. The primary  
 454        purpose of the ID is to determine the charge, momentum, and trajectory of charged particles pass-  
 455        ing through the detector. With this information the ID is also able to precisely determine interaction  
 456        vertices.

457        The ID is composed of three sub-detectors; the Pixel Detector, the Semiconductor Tracker  
 458        (SCT) and the Transition Radiation Tracker (TRT). Figure 4.2 shows the location of these three  
 459        subsystems with respect to each other and the interaction point.

### 460 4.2.1 Pixel Detector

461        The pixel detector is the first detector encountered by particles produced in LHC collisions.  
 462        The original pixel detector consists of 3 barrel layers of silicon pixels, positioned at 5 cm, 9 cm  
 463        and 12 cm from the beamline. There are also 3 disks on each end-cap positioned 50 - 65 cm from  
 464        the interaction point, providing full coverage for  $|\eta| < 2.2$ . The layers are comprised of silicon  
 465        pixels each measuring  $50 \times 400 \mu\text{m}^2$ , with 140 million pixels in total. The pixels are organized  
 466        into modules, which each contain a set of radiation hard readout electronics chips. In 2014, the  
 467        Insertable B-layer (IBL) was installed, creating a new innermost layer of the pixel detector sitting

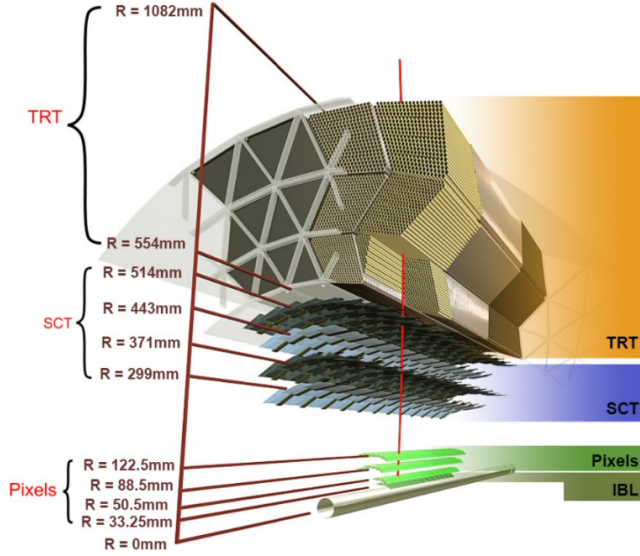


Figure 4.2: A 3D visualization of the structure of the ID in the barrel region [35]

468 just 3.3 cm from the beamline. The pixels of the IBL measure  $50 \mu\text{m}$  by  $250 \mu\text{m}$ , and cover  
 469 a pseudo-rapidity range up to  $|\eta| < 3$ . The IBL upgrade enhances the pixel detector's ability  
 470 to reconstruct secondary vertices associated with short-lived particles such as the b-quark. The  
 471 improved vertex identification also helped compensate for increasing pile-up in Run 2 [34].

#### 472 4.2.2 Semiconductor Tracker

473 The SCT provides at least 4 additional measurements of each charged particle. It employs the  
 474 same silicon technology as the Pixel Detector, but utilizes larger silicon strips which measure  $80 \mu\text{m}$   
 475 by  $12.4 \text{ cm}$ . The SCT is composed of 4 barrel layers, located between 30 cm and 52 cm from  
 476 the beamline, and 9 end-cap layers on each side. The SCT can distinguish tracks that are separated  
 477 by at least  $200 \mu\text{m}$ .

#### 478 4.2.3 Transition Radiation Tracker

479 The TRT provides an additional 36 hits per particle track. The detector relies on gas filled  
 480 straw tubes, a technology which is intrinsically radiation hard. The straws which are each 4 mm in  
 481 diameter and up to 150 cm in length and filled with xenon gas. The detector is composed of about

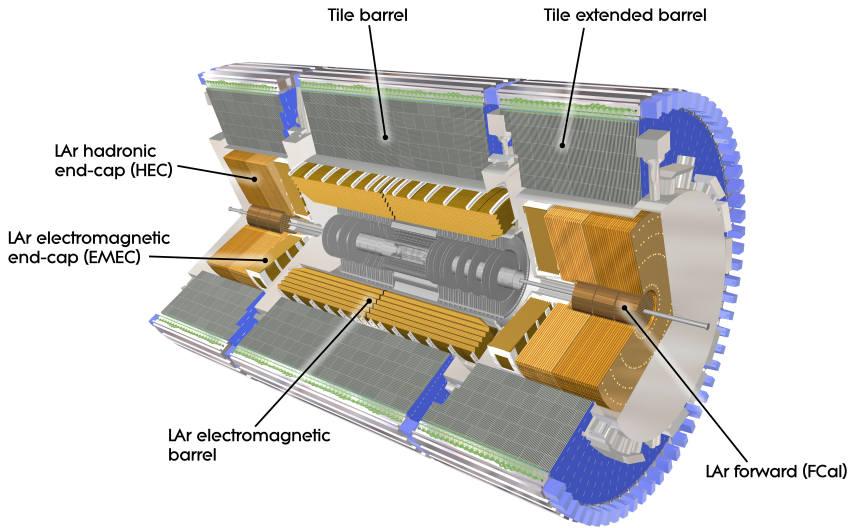


Figure 4.3: ATLAS calorimetry system [36]

482 50000 barrel region straws and 640000 end-cap straws, comprising 420000 electronic readout  
 483 channels. Each channel provides a drift time measurement with a spatial resolution of  $170\ \mu\text{m}$  per  
 484 straw. As charged particles pass through the many layers of the detector, transition radiation is  
 485 emitted. The use of two different drift time thresholds allows the detector to distinguish between  
 486 tracking hits and transition radiation hits.

### 487 4.3 Calorimeters

488 The ATLAS calorimeter system is responsible for measuring the energy of electromagnetically  
 489 interacting and hadronically interacting particles passing through the detector. The calorimeters are  
 490 located just outside the central solenoid magnet, which encloses the inner detectors. The calorime-  
 491 ters also stop most known particles, which the exception of muons and neutrinos, preventing them  
 492 from traveling to the outermost layers of the detector. The ATLAS calorimetry system is composed  
 493 of two subsystems - the Liquid Argon (LAr) calorimeter for electromagnetic calorimetry and the  
 494 Tile calorimeter for hadronic calorimetry. The full calorimetry system is shown in Figure 4.3.

495 4.3.1 Liquid Argon Calorimeter

496 The LAr calorimeter is a sampling calorimeter designed to trigger on and measure the ener-  
497 gies of electromagnetic (EM) particles, as well as hadronic particles in the high  $\eta$  regions. It is  
498 divided in several regions, as shown in Figure 4.3. For the region  $|\eta| < 1.4$ , the electromagnetic  
499 barrel (EMB) is responsible for EM calorimetry, and provides high resolution energy, timing,  
500 and position measurements for electrons and photons passing through the detector. The elec-  
501 tromagnetic endcap (EMEC) provides additional EM calorimetry up to  $|\eta| < 3.2$ . In the re-  
502 gion  $1.4 < |\eta| < 3.2$ , the hadronic endcap (HEC) provides hadronic calorimetry. For hadronic  
503 calorimetry in the region  $|\eta| < 1.4$ , corresponding to a detector radii  $> 2.2$  m, the less expensive  
504 tile calorimeter (discussed in the next section) is used instead. A forward calorimeter (FCAL)  
505 extends the hadronic calorimetry coverage up to  $3.1 < |\eta| < 4.8$  [37].

506 The LAr calorimeter is composed of liquid argon sandwiched between layers of absorber mate-  
507 rial and electrodes. Liquid argon is advantageous as a calorimeter active medium due to its natural  
508 abundance and low cost, chemical stability, radiation tolerance, and linear response over a large  
509 energy range [38]. The calorimeter is cooled to 87k by three cryostats: one barrel cryostat encom-  
510 passing the EMB, and two endcap cryostats. The barrel cryostat also encloses the solenoid which  
511 produces the 2T magnetic field for the inner detector. Front-end electronics are housed outside the  
512 cryostats and are used to process, temporarily store, and transfer the calorimeter signals.

513 **Electromagnetic Calorimeter**

514 For the electromagnetic calorimeters, the layers of electrodes and absorber materials are ar-  
515 ranged in an an accordion shape, as illustrated in Figure 4.4. The accordion shape ensures that  
516 each half barrel is continuous in the azimuthal angle, which is a key feature for ensuring consistent  
517 high resolution measurements. Liquid argon permeates the space between the lead absorber plates,  
518 and a multilayer copper-polymide readout board runs through the center of the liquid argon filled  
519 gap.

520 The detection principle for the LAr calorimeter is the current created by electrons which are

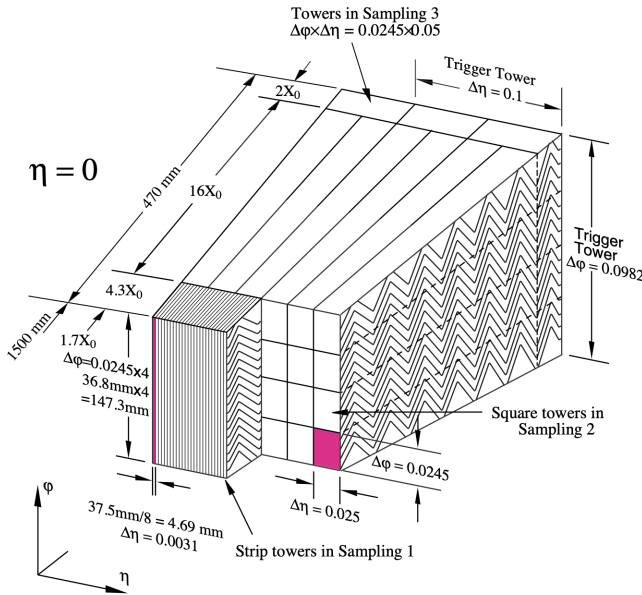


Figure 4.4: Diagram of a segment of the EMB, demonstrating the accordion plate arrangement [37]

521 released when a charged particle ionizes the liquid argon. In the barrel region, the electrons are  
 522 driven towards the center electrodes by a 2000 V potential with a drift time of less than 450 ns [39].  
 523 In the end-caps the voltage varies as a function of the radius in order to maintain a flat response  
 524 [37]. The amount of current produced by the ionized electrons is proportional to the energy of  
 525 the particle creating the signal. Figure 4.5 shows the shape of the signal produced in the LAr  
 526 calorimeter, before and after it undergoes shaping during the readout process. The shaping of the  
 527 pulse enforces a positive peak and a negative tail, which ensures that subsequence pulses can be  
 528 separated with the precision required for the 25 ns LHC bunch spacing [37].

## 529 Hadronic End-cap Calorimeter

530 The HEC sits radially beyond the EMEC. The copper absorber plates in the HEC are oriented  
 531 perpendicular to the beamline, with LAr as the active medium. Each end-cap is divided into two  
 532 independent wheels; the inner wheel uses 25 mm copper plates, while the outer wheel uses 50 mm  
 533 plates as a cost saving measure. In each wheel, the 8.5 mm plate gap is crossed by three parallel